

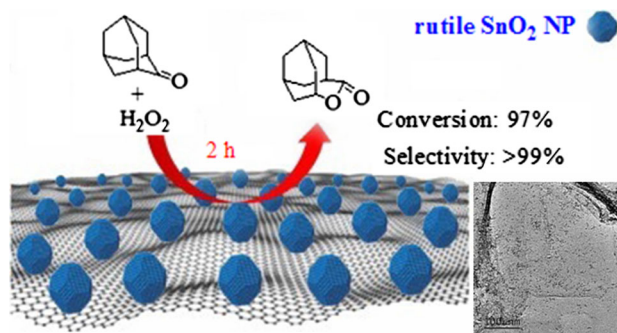
SnO₂ Nanoparticle-Decorated Graphene Oxide Sheets Efficiently Catalyze Baeyer–Villiger Oxidation with H₂O₂

Weiguo Zheng¹ · Rong Tan¹ · Xuanfeng Luo¹ · Chen Xing¹ · Donghong Yin^{1,2}

Received: 9 August 2015 / Accepted: 9 October 2015 / Published online: 18 October 2015
© Springer Science+Business Media New York 2015

Abstract Uniform rutile SnO₂ nanoparticles with small size (*ca.* 3 nm) were highly dispersed on both sides of GO sheets through electrostatic interactions, giving pseudo-homogeneous catalysts of SnO₂/GO nanocomposites. The SnO₂-decorated GO nanocomposites, especially, SnO₂ (15 wt%)/GO was highly efficient and reusable in Baeyer–Villiger oxidation of ketones with H₂O₂.

Graphical Abstract SnO₂/GO nanocomposites, where uniform SnO₂ nanoparticles were tightly gripped on both sides of GO sheets by surface oxygenated functional groups through electrostatic interaction, have proved to be a versatile, efficient and reusable catalyst for the BV oxidation of ketones with H₂O₂.



Keywords Lewis acid catalysis · Heterogeneous catalysis · Oxidation

1 Introduction

B–V oxidation of ketones with H₂O₂ is of great importance in organic chemistry, not only due to the environment friendly oxygen source, but also because obtained lactones or esters are valuable synthetic intermediates in agrochemical, chemical and pharmaceutical industries [1–9]. In 2001, Corma et al. reported the tetravalent tin (Sn^{IV})-containing beta zeolite as a highly active and chemoselective catalyst for B–V oxidation of ketones with H₂O₂ [10]. Sn^{IV} centers, tetrahedrally coordinated in beta zeolite framework, acted as Lewis acids to activate the carbonyl group of ketones through coordination, facilitating the nucleophilic attack on this group by H₂O₂. Despite high yields of lactones, in some cases, microporosity of zeolite hinders the diffusion of bulky molecules, resulting in lower activity and faster deactivation of catalyst [11]. To eliminate the diffusion limitation, mesoporous silica such as

✉ Rong Tan
yiyangtanrong@126.com

✉ Donghong Yin
yindh@hunnu.edu.cn

¹ Key Laboratory of Chemical Biology and Traditional Chinese Medicine Research (Ministry of Education) and Key Laboratory of the Assembly and Application for Organic Functional Molecules, Hunan Normal University, Changsha 410081, People's Republic of China

² Technology Center, China Tobacco Hunan Industrial Corporation, NO. 426 Laodong Road, Changsha 410014, Hunan, People's Republic of China

MCM-41, have been employed to incorporate the Sn^{IV} species [2, 12, 13]. The mesoporous matrix indeed allowed for the free diffusion of reagents, but the amorphous structure of silica wall often incorporates Sn^{IV} species disorderly. As a result, not all Sn^{IV} centers were equally active and/or accessible to the reactants for efficient B–V oxidation [14–16]. Recently, layered double hydroxides (LDHs), a class of two-dimensional anionic clays, have emerged as the alternative support for Sn^{IV} species through ion-exchange [17, 18]. The key structural characteristic that M^{II} and M^{III} cations were distributed in a uniform manner in the hydroxide layers resulted in the formation of Sn^{IV} /LDH with specific morphology/surface structure and high dispersion [19]. Furthermore, ‘flexible’ interlayer spaces of the layered Sn^{IV} /LDH catalyst not only fitted substrates either bulky or less, but also allowed the free access of Sn^{IV} center during reaction. It thus represented a fascinating strategy for developing highly efficient and stable Tin-based catalysts for B–V oxidation with H_2O_2 .

Graphene, a novel layered carbon material with a tight packing of honeycomb lattice, has become one of the rising stars in material science [20]. Its intriguing properties, such as unique layered structure, high surface area, high flexibility and mechanical strength, made it very attractive in heterogeneous catalysis [21–24]. Although many SnO_2 /graphene nanocomposites have been recently proposed as an anode material for Li-ion batteries [25–28], the employment of SnO_2 /graphene nanocomposites in catalysis was scarcely reported. For higher catalytic performance, it was desirable to have smaller particle size and higher dispersion of SnO_2 NPs in the composite. However, it was difficult to control the dispersion state of loaded NPs on graphene surfaces, mainly due to the lack of strong interactions between them [29]. Furthermore, layer graphene sheets tended to stack with each other in solution, thus losing their high surface area and intrinsic chemical and physical properties. An ideal solution to above problems was supporting SnO_2 NPs on a graphene oxide (GO) sheet instead of a graphene sheet. Different from graphene, GO sheet consisted of intact graphitic regions interspersed with sp^3 -hybridized carbons containing carboxyl, hydroxyl, and epoxide functional groups on the edge, top, and bottom surface of each sheet. The abundant surface oxygenated functional groups ensured GO to grip SnO_2 NPs tight on the surface through electrostatic interactions, which prevented not only the aggregation of SnO_2 NPs, but also the aggregation of graphene sheets. In addition, all the SnO_2 NPs located on the GO surface were exposed to the reagents in catalysis, which may further enhance the catalytic efficiency of SnO_2 /GO nanocomposites.

Herein, SnO_2 NPs were grown on the GO surfaces via a hydrothermal method using $\text{SnCl}_4 \cdot 5\text{H}_2\text{O}$ as a metal precursor. Then SnO_2 NPs were formed, in situ, and anchored

by the oxygenate groups on the GO layer, forming uniform loading of SnO_2 NPs on GO sheets. It has proved that SnO_2 NPs were kept small in size and dispersed uniformly on the GO sheets. The resultant SnO_2 /GO nanocomposites were demonstrated the efficient and selective solid Lewis acid catalysts for B–V oxidation with H_2O_2 . Quantitative yield of lactones was obtained within 2 h even in the case of bulky 2-adamantanone. Furthermore, the catalyst could be easily separated for reuse by centrifugation.

2 Experimental

2.1 Materials and Methods

Cyclopentanone and high-purity graphite (99.9999 %, 200 mesh) were purchased from Alfa Aesar. Cyclohexanone and adamantanone were obtained by J&K. Other commercially available chemicals were laboratory grade reagents from local suppliers. All of the solvents were purified by standard procedures.

Surface structure of the samples was measured using a TEM (JEOL JEM-3010). X-ray diffraction (XRD) patterns were recorded on a Philips X'PERT-Pro-MPD diffractometer using $\text{Cu K}\alpha$ radiation ($\lambda = 1.542 \text{ \AA}$). A continuous scan mode was used to collect the 2θ from 5° to 80° . X-ray Photoelectron Spectroscopy (XPS) data were obtained with an ESCALab220i-XL electron spectrometer from VG Scientific using 300 W $\text{Al K}\alpha$ radiation. The base pressure was about 3×10^{-7} Pa. SnO_2 NPs contents were analyzed by TGA using a NETZSCH STA 449C thermal analyzer. Samples (*ca.* 0.01 g) were heated from room temperature up to 800°C with 10 K/min under air flow using alumina sample holders. Thin layer chromatography (TLC) was conducted on glass plates coated with silica gel GF₂₅₄. The conversion and ee values were measured by a 6890 N gas chromatograph (Agilent Co.) equipped with a capillary column (HP19091G-B213, 30 m \times 0.32 mm \times 0.25 μm).

2.2 Preparation of $\text{SnO}_2(x)$ /GO (Where x is the Mass Ratio of SnO_2 NPs)

GO was prepared by the oxidation of high-purity graphite powder (99.9999 %, 200 mesh) with $\text{H}_2\text{SO}_4/\text{KMnO}_4$ according to the Hummers method [30], and then was subjected to dialysis for 7 days to completely remove metal ions and acids. The resulting product was dried at room temperature under vacuum overnight, giving GO as yellowish-brown powder. FT-IR (KBr): 3187, 3132, 1735, 1621, 1224, 1050 and 581 cm^{-1} .

The dried GO (1.0 g) was sonicated in deionized water (100 mL) for 0.5 h to ensure most GO being fully exfoliated.

Various amount of SnCl₄·5H₂O (0.125, 0.25, 0.375, 0.50 and 0.75 g) in deionized water (50 mL) was then added into the homogeneous dispersion. After further ultrasonic treatment for 0.5 h, the mixtures were refluxed at 100 °C for 24 h, resulting in a black suspension. The precipitate was collected by centrifugation and washed with deionized water. The products were dried at room temperature overnight under vacuum, giving SnO₂/GO nanocomposites with various SnO₂ loading (*ca.* 7.5, 15, 20, 30 or 40 wt%).

2.3 B–V Oxidation of Ketones with H₂O₂

SnO₂/GO nanocomposites (0.05 g) and ketones (1.0 mmol) were mixed in 1,2-dichloroethane (15 mL) under vigorously stirring. H₂O₂ (30 wt%, 2.0 mmol) was then added dropwise at 90 °C. The reaction progress was monitored by GC. After the reaction, catalyst was separated by centrifugation. The liquid reaction mixture was extracted by ethyl ether and then quantitatively analyzed by a 6890 N gas chromatograph (Agilent Co.) equipped with the capillary column (HP19091G-B213, 30 m × 0.32 mm × 0.25 μm). The recovered catalyst was washed with ethanol and distilled water repeatedly, and dried at 40 °C overnight for reused.

3 Results and Discussions

3.1 Preparation of SnO₂/GO Nanocomposites

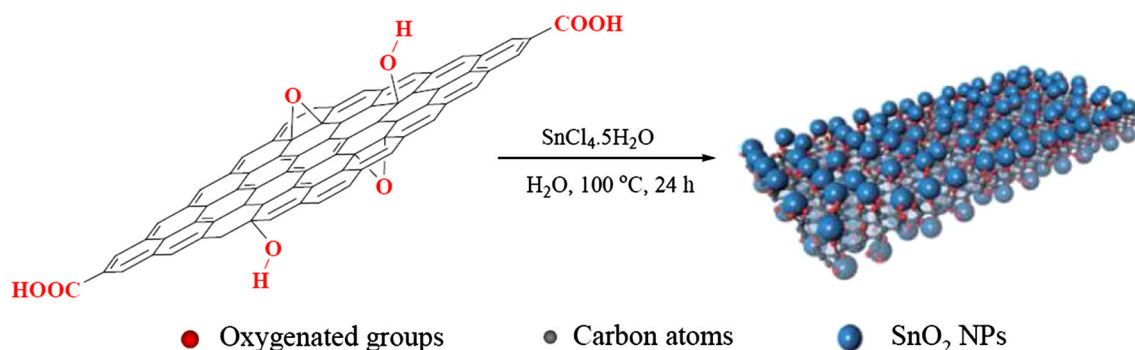
GO, an oxygenated derivative of graphene, contains abundant oxygen-containing groups such as carboxyl, carbonyl, hydroxyl and ether on the surface. The oxygen-containing groups were capable of gripping metal oxide NPs through electrostatic interactions, which thus facilitated high dispersion of metal oxide NPs on both sides of GO sheet, and also prevented them from aggregation [31–33]. With this point in mind, we decided to locate SnO₂ NPs on the surface of GO sheets through electrostatic interactions between the oxygenated functional groups and SnO₂ NPs. A convenient

hydrothermal method was employed for the hybridization, as shown in Scheme 1. GO sheets were readily dispersed in water due to surface oxygenate species, forming a uniform GO nanosheets suspension. When GO solution was mixed with SnCl₄·5H₂O solution, the Sn^{IV} cation was selectively bonded with the negative oxygenated groups by electrostatic force. After incubated at 100 °C for 24 h, anchored Sn^{IV} cation was in situ converted to SnO₂ NPs, and gripped by the oxygenated functional groups through electrostatic interaction. The driving force for the gripping of SnO₂ NPs in the nanocomposite structures may be subdivided into the following categories: (I) dative bonds between oxygen atom in oxygenated functional groups and Sn atoms of SnO₂, (II) hydrogen-bond between oxygen atom of SnO₂ NPs and hydrogen atom in hydrogen-containing oxygenated functional groups. As a result, uniform SnO₂ NPs with small size should be highly dispersed on both sides of GO sheets, as proposed in Scheme 1. This unique hybrid architecture gave rise to an efficient and stable Lewis acid catalyst for B–V oxidation.

3.2 Characterization of Samples

3.2.1 XPS

XPS was employed as an optimal characterization technique to provide the direct evidence for the conjugation of SnO₂ NPs and GO nanosheets (Fig. 1). Figure 1a shows the XPS survey spectra of GO and typical SnO₂(15 wt%)/GO nanocomposite, which were normalized with respect to the respective C 1s peaks. Obviously, besides C (C 1s, 286.1 eV) and O (O 1s, 532.0 eV) peaks [34, 35], the nanocomposite exhibited typical Sn (Sn 3p, 3d, 4s, 4p, 4d) signals in the survey spectrum [36], suggesting the existence of Tin species on GO sheets. The Sn 3d XPS spectrum of composite was presented in Fig. 1b, where the peaks of Sn 3d_{5/2} (487.20 eV) and Sn 3d_{3/2} (495.53 eV) were distinct. They had a spin energy separation of 8.33 eV and an area ratio of 1:1.5, which were in good accordance with the reported XPS data of SnO₂ [37, 38]. It suggested that SnO₂ NPs were in situ



Scheme 1 Schematic representation of SnO₂ NPs loaded on GO through hydrothermal method

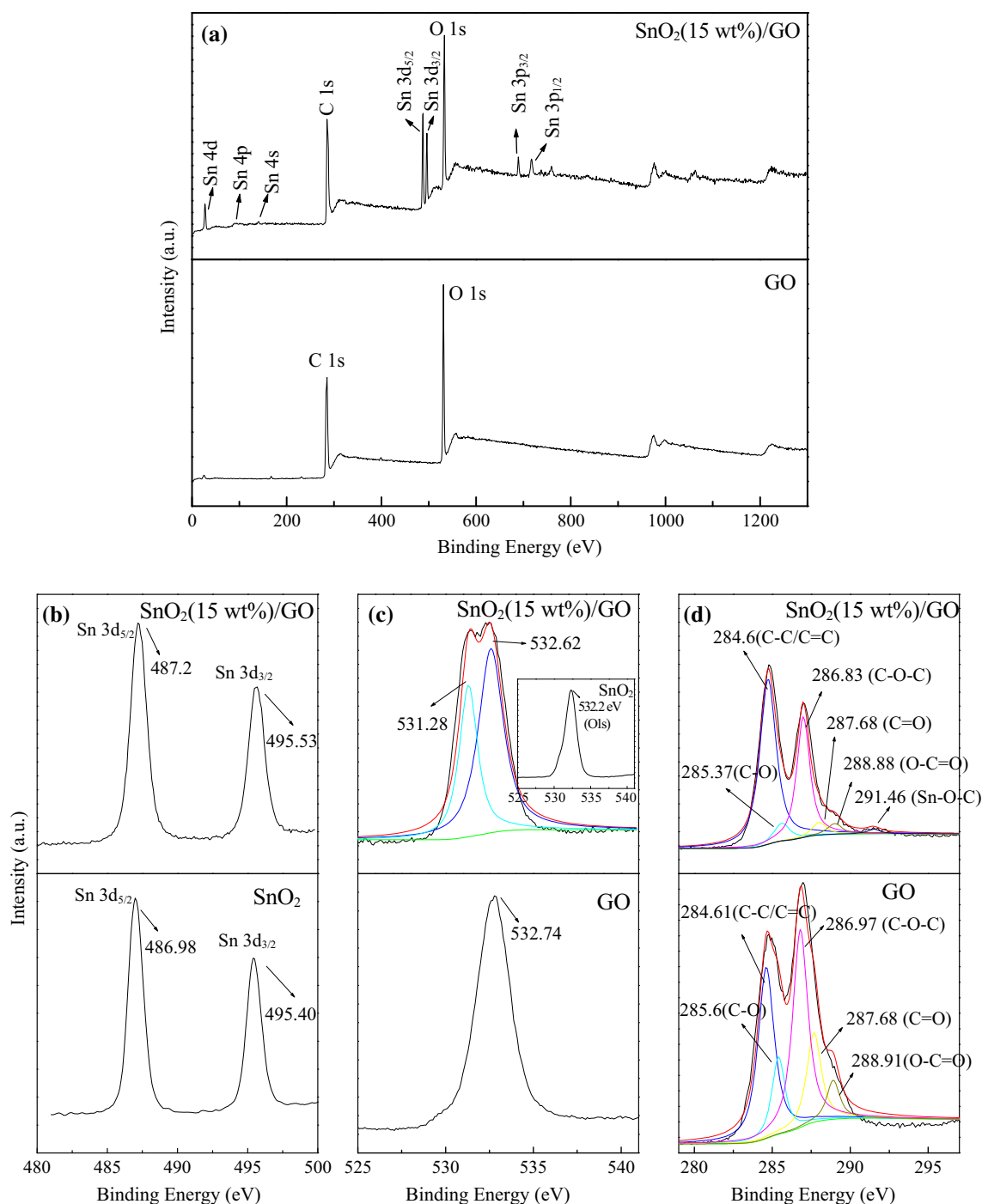


Fig. 1 XPS survey spectra of SnO₂(15 wt%)/GO and GO (a), Sn3d XPS spectra of SnO₂(15 wt%)/GO and commercial SnO₂ NPs (b), O1s XPS spectra of SnO₂(15 wt%)/GO and GO (c), and C1s XPS spectra of SnO₂(15 wt%)/GO and GO (d)

grown on GO surfaces during hydrothermal synthesis. While, we noticed that the obtained nanocomposite showed slight increase in binding energy of Sn 3d, as compared with commercial SnO₂ NPs (Fig. 1b). Higher binding energy should be related with the coordination between oxygenated functional groups of GO and Sn atoms of SnO₂. The deduction could also be drawn from the evidence that the O1s

binding energy of oxygenated functional groups in SnO₂/GO composite, shifted from 532.74 to 532.62 eV, compared with that in GO (Fig. 1c). Furthermore, an additional O1s signal (531.28 eV) associated with O-Sn^{IV} species of SnO₂ [39] was also observed in the O1s XPS spectrum of SnO₂(15 wt%)/GO composite. This was unambiguous evidence for a SnO₂/GO composite structure. Notably, the O1s

binding energy (531.28 eV, Fig. 1c) of O–Sn^{IV} species in nanocomposite slightly decreased as compared with that in commercial SnO₂ NPs (532.20 eV, Fig. 1c inset). It was probably due to a hydrogen-bonding between oxygen atom of the SnO₂ NPs and the hydrogen atom of hydrogen-containing oxygenated functional groups on GO sheets. We could thus deduce that SnO₂ NPs were tightly bonded to the GO layer by oxygenate groups through dative bond and/or hydrogen bond. Actually, similar interactions have been reported in other metal oxide/GO hybrids, such as CuO/GO [40], MnO₂/GO [41], and Fe₃O₄/GO [31] etc. These facts were consistent with the synthesis design, and confirmed the successful dispersion of SnO₂ NPs on the basal planes of GO nanosheets, as shown in Scheme 1.

Figure 1d showed the C1s deconvolution spectra of SnO₂(15 wt%)/GO composite and pristine GO. As compared with GO, the C1s XPS spectrum of SnO₂/GO nanocomposite exhibited an additional C1s signal at 291.46 eV, which was probably associated with the Sn–O–C carbonaceous bonds due to the interaction between Sn atom and oxygen-containing functional groups of GO as mentioned above. Moreover, decreased intensity of carbon binding to oxygenated functional groups was observed in the C1s XPS spectrum of SnO₂/GO. Such results indicate that partial oxygen-containing functional groups were eliminated during the hydrothermal process. It thus tuned a hydrophobic surrounding for SnO₂ NPs, suppressing the undesired competitive coordination of water to the Lewis acid center. The remaining oxygenated groups helped to grip metal oxide NPs tight on the GO surface through electrostatic interactions, which were crucial to the high dispersion of SnO₂ NPs on GO sheets.

3.2.2 XRD

The crystal structure of SnO₂ NPs placed on GO sheets was determined by XRD. Figure 2 shows powder XRD patterns of SnO₂/GO nanocomposites and pristine GO material. Obviously, pristine GO displayed a strong (002) peak (*) centered at 10.5°, suggesting the layered structure with an average interlayer distances of ca. 0.85 nm (Fig. 2a). While, the sharp diffraction peak disappeared, accompanied by the appearance of several new peaks (#) at 2θ of 26.56, 34.22, 51.50, and 65.42° in XRD patterns of SnO₂(x)/GO nanocomposites (Fig. 2b–e), which were attributed to (100), (101), (211), and (112) planes of tetragonal rutile SnO₂ (JCPDS Card No. 41-1049), respectively [28, 42]. Therefore, rutile SnO₂ crystals were deposited on GO sheets during the hydrothermal process, and layer-stacking regularity of GO sheets was disturbed by the decorated rutile SnO₂ NPs. The exfoliated GO sheets should be beneficial for free access of SnO₂ NPs to reagents during the oxidation. An average crystal size of

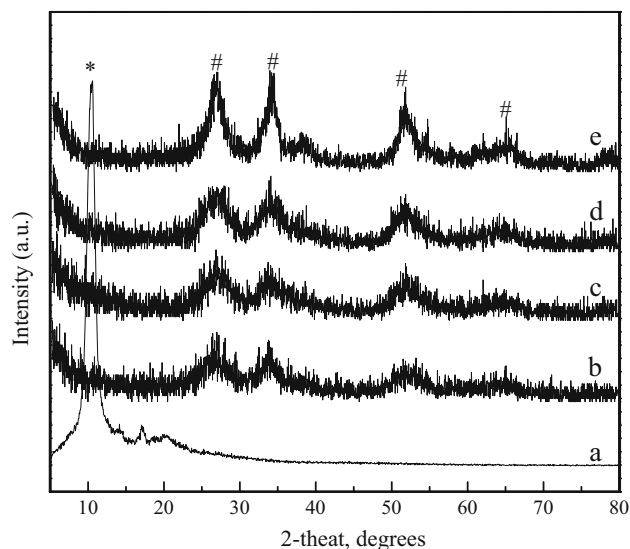


Fig. 2 XRD patterns of GO (a), SnO₂(15 wt%)/GO (b), SnO₂(20 wt%)/GO (c), SnO₂(30 wt%)/GO (d), and SnO₂(40 wt%)/GO (e)

SnO₂ in typical SnO₂(15 wt%)/GO was estimated using Scherrer equation of $d = K\lambda/\beta\cos\theta$ and was found to be 2.6 nm at $2\theta = 26.56^\circ$, where d is the average crystal size, $K = 0.89$ is the Scherrer constant, $\lambda = 0.154$ nm is the wavelength of X-ray, β is the width (in radian) of the XRD peak at half maximum intensity and $\theta = 26.56^\circ/2$ is the Bragg diffraction angle found from XRD data.

3.2.3 Morphological Analyses

The high dispersion of uniform SnO₂ NPs on exfoliated GO sheets was further proved by morphological analyses. Figure 3 shows the TEM images of SnO₂/GO nanocomposites with various SnO₂ loading. Obviously, TEM image of SnO₂(15 wt%)/GO showed thin layered GO sheets, on which uniform SnO₂ NPs were distributed homogeneously with the size of ca. 3 nm (Fig. 3b). The size obtained from TEM was approach to that determined by XRD (2.6 nm). It was direct visual evidence that SnO₂ NPs were evenly anchored by the oxygenated groups on GO surface rather than disordered physical adsorption on the basal planes. The strong interaction between them prevents the NPs from aggregating and increases the stability of SnO₂ NPs. As the oxygenate groups are uniformly distributed on two sides of the GO sheets, SnO₂ NPs should be gripped on both sides of GO sheets, resulting in a sandwich-like structure where layer of GO sheet alternated by SnO₂ NPs sheet. Aggregation problem of GO could be also prevented or at least minimized, which should be beneficial for mass transfer during the heterogeneous catalysis. Increasing the mass ratio of SnO₂ from 15 to 40 wt% led to the aggregation or even accumulation of NPs on the basal planes (Fig. 3b–e). It was probably

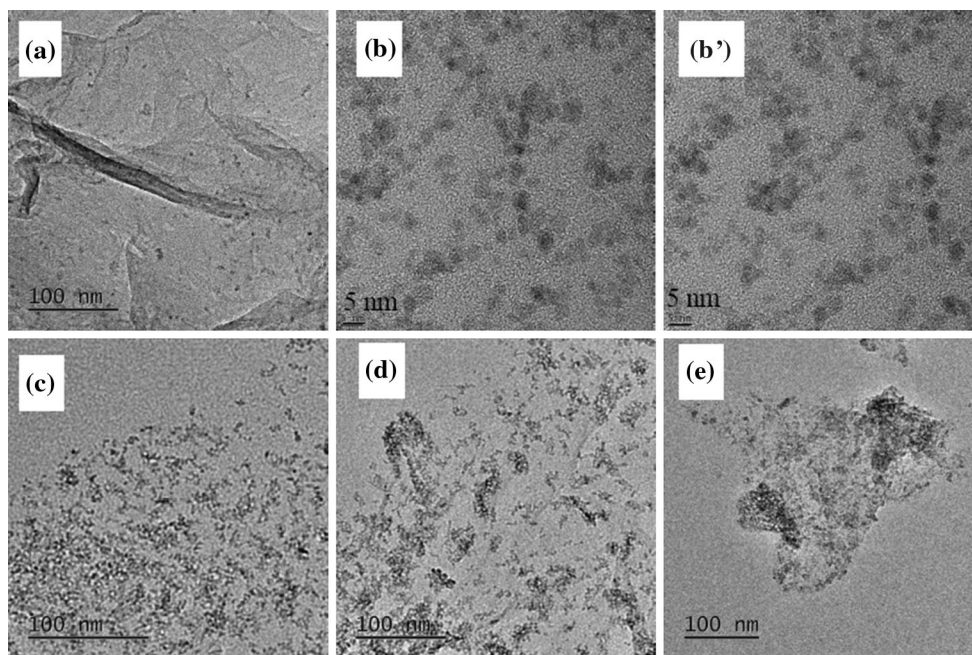
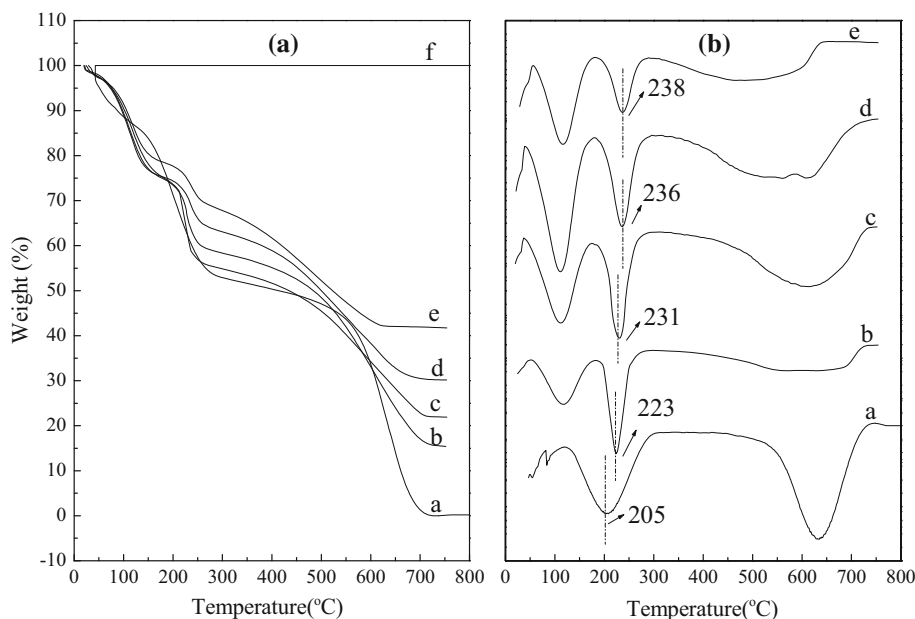


Fig. 3 TEM images of SnO₂(7.5 wt%)/GO (a), SnO₂(15 wt%)/GO fresh (b) and recovered after 10 times (b'), SnO₂(20 wt%)/GO (c), SnO₂(30 wt%)/GO (d), and SnO₂(40 wt%)/GO (e)

Fig. 4 Thermogravimetric (a) and differential thermogravimetric (b) profiles of the pristine GO (a), SnO₂(15 wt%)/GO (b), SnO₂(20 wt%)/GO (c), SnO₂(30 wt%)/GO (d), and SnO₂(40 wt%)/GO (e), and commercial SnO₂ NPs (f) under air atmosphere



due to that SnO₂ Nps were too much to be gripped by the surface oxygenated groups. Sparse SnO₂ Nps was observed on the GO sheets when mass ratio of SnO₂ decreased to 7.5 wt% (Fig. 3a). Low local concentration of active sites was detrimental to efficient catalysis. Therefore, SnO₂(15 wt%)/GO composite has the most reasonable structure that sufficient uniform SnO₂ NPs were homogeneously distributed onto GO sheets, which led to highly efficient solid Lewis acid catalyst for B–V oxidation with H₂O₂.

3.2.4 TGA

Thermal analysis was performed to assess the thermal decomposition behaviour of SnO₂/GO nanocomposites, as well as to quantify the mass percentage of SnO₂ in the nanocomposites. The results obtained are depicted in Fig. 4. Pristine GO sheets exhibited three distinct steps of weight loss in the combined TG–DTG curves (Fig. 4a). The first weight loss before 100 °C corresponded to

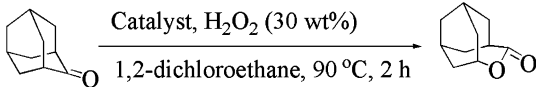
removal of the surface-adsorbed and/or interlayer water molecules. A second large weight loss centered at 205 °C, which was assigned to the pyrolysis of the labile oxygen-containing functional groups [43]. The third step assigned to the successive cleavage of carbon sketch appeared at 550 °C. The weight loss extended up to ca. 730 °C until the GO was completely decomposed under air flow. A similar thermal behaviour was observed for the SnO₂/GO samples (Fig. 4b–e). Three mass loss steps associated with the removal of water molecules, oxygen-containing functional groups and carbon sketch are distinguished in the combined TG–DTG curves of SnO₂/GO samples. The non-removable residue belonged to incorporated SnO₂ NPs which was quite stable with negative mass loss during the temperature range (Fig. 4f). Thus, the mass percentages of SnO₂ in corresponding composites could be accordingly estimated to be 15 (Fig. 4b), 20 (Fig. 4c), 30 (Fig. 4d) and 40 (Fig. 4e) wt%, respectively. Furthermore, we noticed that the decomposition temperature of oxygenated groups gradually increases with the increase of SnO₂ content in composites (Fig. 4b–e). The observation suggested the interaction between SnO₂ NPs and oxygenated groups, which enhanced thermal stability of the oxygen-containing functional groups.

3.3 Catalytic Performances

The featured structure that small sized SnO₂ NPs are uniformly dispersed on the surface of GO sheets turns the SnO₂/GO nanocomposite into the efficient solid Lewis acid catalysts for the B–V oxidation of ketones with H₂O₂. The catalytic efficiency of the resultant SnO₂/GO nanocomposite catalyst was investigated in B–V of bulky 2-adamantanone with H₂O₂ (30 wt%) in 1,2-dichloroethane at 90 °C. The results are presented in Table 1. GO material and commercial SnO₂ NPs were also examined for comparison purposes.

Obviously, commercial SnO₂ NPs were inactive in B–V oxidation with H₂O₂, giving practically no lactone of 2-oxatricyclo [4. 3. 1. 1^{4,8}]-undecan-9-one even if double H₂O₂ was used (Table 1, entry 1). While, the catalytic efficiency benefited from dispersing SnO₂ NPs on GO sheets, although GO itself was also inactive (Table 1, entry 2). 48–97 % Conversion of 2-adamantanone was obtained over the obtained SnO₂/GO nanocomposites (Table 1, entries 3–7). The results demonstrated the positive effect of GO sheets on catalytic performance of SnO₂(x)/GO nanocomposites. Abundant oxygenate groups on GO sheets ensured high dispersion of uniform SnO₂ NPs on both sides of the GO layer with small size. Delamination of the nanocomposites allowed catalytic reactions to be carried out under pseudo-homogeneous reaction conditions, thereby significantly increasing the reaction rate. More

Table 1 Results of the B–V oxidation of 2-adamantanone with H₂O₂ over different catalysts



Entry	Catalyst	Conversion ^a (%)	Selectivity ^a (%)
1	SnO ₂	Trace	/
2	GO	Trace	/
3	SnO ₂ (7.5 wt%)/GO	56	>99
4	SnO ₂ (15 wt%)/GO	97	>99
5	SnO ₂ (20 wt%)/GO	70	>99
6	SnO ₂ (30 wt%)/GO	55	>99
7	SnO ₂ (40 wt%)/GO	48	>99
8	SnO ₂ -MCM-41 ^b	3 ^c	96 ^c

Catalyst (0.025 g), 2-adamantanone (1.0 mmol), H₂O₂ (30 wt%, 2.0 mmol), 1,2-dichloroethane (2 mL), 2 h, 90 °C

^a Determined by GC

^b Catalyst (0.66 mol% of Sn with respect to the ketone), 2-adamantanone (1 mmol), H₂O₂ (50 wt%, 1.5 mmol), dioxane (3 g), 16 h, 75 °C

^c Data from the Ref. [5]

importantly, the synergistic effect between SnO₂ NPs and GO support effectively promoted further enhancement of catalytic activity. The deduction can be drawn from the evidence that SnO₂ directly grafted onto mesoporous MCM-41 yielded negligible 2-adamantanone conversion under analogous reaction conditions (Table 1, entry 8), as reported by Román-Leshkov et al. [5]. Notably, SnO₂/GO nanocomposite containing 15 wt% SnO₂ NPs showed the most remarkable activity in the B–V oxidation. Almost quantitative conversion of 2-adamantanone with excellent selectivity to lactone (>99 %) was achieved over 0.025 g of SnO₂ (15 wt%)/GO nanocomposite (2.0 mol%, regarding catalytic Tin sites) within 2 h (Table 1, entry 4). While, the conversion gradually decreased as SnO₂ loading increased (Table 1, entries 4–7). Only 48 % conversion of 2-adamantanone was observed when SnO₂ loading was increased to 40 wt% (Table 1, entry 7). Higher loading of SnO₂ resulted in the lower dispersion state of SnO₂ NPs, as shown in TEM images, which was detrimental to the catalysis. These results thus prompted us to further decrease SnO₂ loading from 15 to 7.5 wt%. Unexpectedly, although uniform NPs, SnO₂ (7.5 wt%)/GO nanocomposite was unsatisfied for the B–V oxidation of 2-adamantanone, likely due to the insufficient active sites (Table 1, entry 3). Interestingly, the selectivity to lactone was almost 100 % irrespective of the Tin concentration with no formation of any side-products.

Apart from enhanced catalytic efficiency, the reusability of SnO₂/GO composites in B–V oxidation was also enjoyable. Typical SnO₂(15 wt%)/GO nanocomposite was

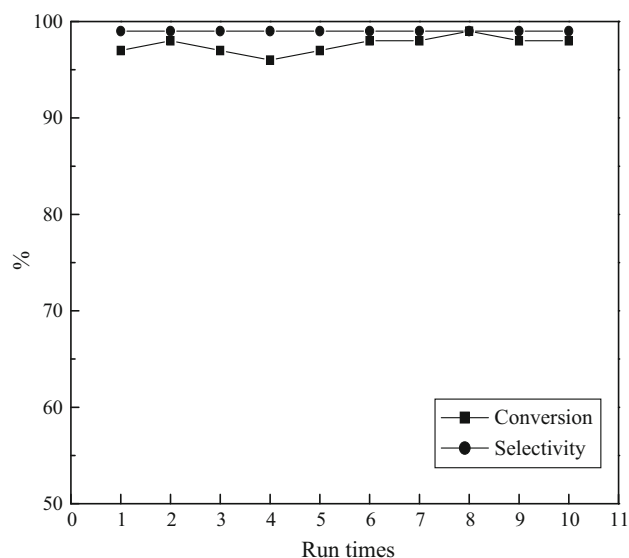


Fig. 5 Reusability of SnO₂(15 wt%)/GO in the B–V oxidation of 2-adamantanone with H₂O₂

employed to investigate the reusability in B–V oxidation of 2-adamantanone with H₂O₂, and the results were listed in Fig. 5. Simply by centrifugation, the SnO₂(15 wt%)/GO catalyst could be facilely recovered for reuse. To our delight, it could be reused for at least ten times with no appreciable decrease in catalytic activity and selectivity. Therefore, the SnO₂(15 wt%)/GO catalyst was quite stable in the oxidation. The stability was further identified by TEM image of recovered SnO₂(15 wt%)/GO nanocomposite (Fig. 3b' vs b). No significant change in layered structure of catalyst, as well as dispersed state and particle size of SnO₂ NPs was observed even after reused for ten times. The results indicated that tightly pinning SnO₂ NPs on GO sheets could effectively enhance the dimensional stability of NPs during cycling. Leaching of

SnO₂ NPs was also avoided by the electrostatic interaction between SnO₂ NPs and oxygenated groups on GO sheets, as indicated by the identical SnO₂ content in recovered catalyst (15 wt% loading). More importantly, the organic deposits, a main reason for poisoning the Tin-containing catalyst [11, 12], can also be avoided because of the free traffic of reactants and products in the layered SnO₂/GO nanocomposite. Therefore, the novel SnO₂(15 wt%)/GO nanocomposite was efficient and reusable in the typical B–V oxidation of 2-adamantanone with H₂O₂.

It should be more attractive if the nanocomposite can be applied to various ketones. Table 2 summarized the B–V oxidation of various ketones in the presence of SnO₂(15 wt%)/GO. Besides 2-adamantanone, cyclobutanone was also successfully oxidized to lactone with high efficiency and excellent selectivity under identical condition (Table 2, entry 2). The oxidation of other cyclic ketones (5- or 6- membered rings) also occurred smoothly to afford the corresponding lactones with excellent selectivity, although longer reaction time was required (Table 2, entries 4, 6, and 8). Interestingly, the substituent in six-membered cyclic ketone influenced the conversion of ketone in B–V oxidation (Table 2, entries 7 and 8). Cyclohexanone with methyl substituent at para-position was less reactive than cyclohexanone, due to the steric effect, as well as electron-donating inductive effect of methyl group (Table 2, entry 8 vs 6). Notably, although the reaction rate depends on the chemical structure of ketones, it can be concluded that the SnO₂(15 wt%)/GO nanocomposite could oxidize the various ketones to corresponding lactones with excellent selectivity (>99 %) (Table 2, entries 1, 2, 4, 6, and 8). The high selectivity obtained is attributed to the carbonyl group activation mechanism proposed by Corma et al., which involves initial selective activation of the carbonyl group, followed by reaction with non-activated H₂O₂ [10].

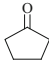
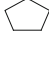
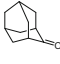
Table 2 Results of B–V oxidation of various ketones with H₂O₂ over SnO₂ (15 wt%)/GO nanocomposite

Entry	Substrate	Product	Time (h)	Conversion ^a (%)	Selectivity ^a (%)
1			2	97	>99
2			2	99	>99
3			2	73	>99
4			6	92	>99
5			2	56	>99
6			6	91	>99
7			2	43	>99
8			16	95	>99

SnO₂ (15 wt%)/GO (0.025 g, 2 mol% of Sn with respect to the ketone), substrate (1 mmol), H₂O₂ (30 wt%, 2 mmol), 1,2-dichloroethane (2 mL), 2 h, 90 °C

^a The same as Table 1

Table 3 Comparison of results obtained over different catalysts in the B–V oxidation with H₂O₂

Entry	Catalyst	Substrate	Conv. ^a (%)	Sel. ^a (%)	Ref.
1	SnO ₂ (15 wt%)/GO		92	>99	This work
2	Sn-Montmorillonite		45	100	Ref. ^b
3	Sn-palygorskite		81	100	Ref. ^c
4	Sn/PS		22	100	Ref. ^d
5	Silica-AlCl ₃		37	75	Ref. ^e
6	SnO ₂ (15wt%)/GO		97	>99	This work
7	Sn/MCM-41		49	91	Ref. ^f
8	Sn/MSNSs		89	98	Ref. ^f

Catalyst (0.025 g), 2-adamantanone (1.0 mmol), H₂O₂ (30 wt%, 2.0 mmol), 1,2-dichloroethane (2 mL), 2 h, 90 °C

^a Determined by GC

^b Data from the Ref. [44]

^d Data from the Ref. [18]

^c Data from the Ref. [45]

^e Data from the Ref. [46]

^f Data from the Ref. [10]

Superiority of the SnO₂(15 wt%)/GO nanocomposite over other reported catalysts, such as Sn-Montmorillonite [44], Sn-palygorskite [18], Sn/PS [45], and Silica-AlCl₃, is seen in Table 3. Obviously, SnO₂(15 wt%)/GO was far more efficient than these reported catalysts either layered or porous in B–V oxidation of cyclopentanone with H₂O₂, due to the pseudo-homogeneous reaction conditions, as well as synergistic effect between SnO₂ NPs and GO support (Table 3, entry 1 vs entries 2–5). Especially, silica-AlCl₃ gave only 37 % conversion of cyclopentanone with low selectivity (70 %) to lactone (Table 3, entry 5). Furthermore, SnO₂(15 wt%)/GO nanocomposite also exhibited much higher activity than tin containing mesoporous silicas even in the case of bulky 2-adamantanone (Table 3, entry 6 vs entries 7, 8) [10]. The results demonstrated the advantages of SnO₂/GO nanocomposite used for baeyer-villiger oxidation reaction. Apart from higher efficiency, the reusability of SnO₂(15 wt%)/GO was also superior to that of the compared catalysts. Blocking of the active sites by either products or intermediates, a main reason for deactivation of the Tin-containing catalyst, was avoided by the flexible layered structure of SnO₂/GO nanocomposite. Furthermore, leaching of SnO₂ NPs was also minimized due to the electrostatic interaction between SnO₂ NPs and oxygenated groups on GO sheets.

4 Conclusions

With the aid of oxygenated functional groups, small rutile SnO₂ NPs (*ca.* 3 nm) have been controllably anchored on GO sheets evenly and tightly for the formation of SnO₂/GO nanocomposites. Characterization results confirmed the

loading of SnO₂ NPs on both sides of the exfoliated GO sheets through electrostatic interactions. Benefiting from the flexible GO support, high dispersion of SnO₂ NPs, as well as the intimate interaction between SnO₂ NPs and GO, the resultant SnO₂/GO composites, especially SnO₂(15 wt%)/GO, exhibited excellent performance as the solid Lewis acid catalysts in B–V oxidation of ketones with H₂O₂. Furthermore, catalyst poisoning by organic deposits could also be effectively avoided by free traffic of reactants and products in the layered SnO₂/GO nanocomposite. The heterogeneous catalyst was stable in the reaction system and could be easily recovered for efficient reuse. The design and controlled synthesis of SnO₂/GO nanocomposites provided a facile, economic, and versatile approach to promote the catalytic performance of other metal oxides and can be scaled up easily for industrial production.

Acknowledgments The project was financially supported by the National Natural Science Foundation of China (Grant No. 21476069), the Scientific Research Fund of Hunan Provincial Education Department (13B072), the Program for Excellent Talents in Hunan Normal University (ET14103), the Hunan Provincial Innovation Foundation for Postgraduate (CX2013B209) and the Program for Science and Technology Innovative Research Team in Higher Educational Institutions of Hunan Province.

References

- Conte V, Floris B, Galloni P, Mirruzzo V, Scarso A, Sordi D, Strukul G (2005) *Green Chem* 7:262
- Jiménez-Sanchidrián C, Ruiz JR (2008) *Tetrahedron* 64:2011
- Sasakura N, Nakano K, Ichikawa Y, Kotsuki H (2012) *RSC Adv* 2:6135
- Hammond C, Conrad S, Hermans I (2012) *Angew Chem Int Ed* 51:11736

5. Luo Y, Bui L, Gunther WR, Min E, Román-Leshkov Y (2012) *ACS Catal* 2:2695
6. Hara T, Hatakeyama M, Kim A, Ichikuni N, Shimazu S (2012) *Green Chem* 14:771
7. Ma Q, Xing W, Xu J, Peng X (2014) *Catal Commun* 53:5
8. Uyanik M, Ishihara K (2013) *ACS Catal* 3:513
9. Chen S, Zhou X, Li Y, Luo R, Ji H (2014) *Chem Eng J* 41:138
10. Corma A, Nemeth LT, Renz M, Valencia S (2001) *Nature* 412:423
11. Wang Y, Yokoi T, Otomo R, Kondo JN, Tatsumi T (2015) *Appl Catal A* 490:93
12. Corma A, Navarro MT, Nemeth L, Renz M (2001) *Chem Commun* 21:2190
13. Corma A, Navarro MT, Renz M (2003) *J Catal* 219:242
14. Li L, Stroobants C, Lin KF, Jacobs PA, Sels BF, Pescarmona PP (2011) *Green Chem* 13:1175
15. Osmundsen CM, Holm MS, Dahl S, Taarning E (2012) *Proc R Soc A* 468:2000
16. Cho HJ, Dornath P, Fan W (2014) *ACS Catal* 4:2029
17. Pillai UR, Sahle-Demessie E (2003) *J Mol Catal A* 191:93
18. Lei Z, Zhang Q, Luo J, He X (2005) *Tetrahedron Lett* 46:3505
19. He S, An Z, Wei M, Evans DG, Duan X (2013) *Chem Commun* 49:5912
20. Stankovich S, Dikin DA, Dommett GHB, Kohlhaas KM, Zimney EJ, Stach EA, Piner RD, Nguyen ST, Ruoff RS (2006) *Nature* 422:282
21. Kakaei K, Dorraji M (2014) *Electrochim Acta* 143:207
22. Kakaei K (2015) *Electrochim Acta* 165:330
23. Lan D, Yang F, Luo S, Au C, Yin S (2014) *Carbon* 73:351
24. Zheng W, Tan R, Yin S, Zhang Y, Zhao G, Chen Y, Yin D (2015) *Catal Sci Technol* 5:2092
25. Tan C, Zhao S, Yang G, Hu S, Qin X (2015) *Ionics* 21:987
26. Thomas R, Rao KY, Rao GM (2014) *Mater Express* 4:65
27. Patil S, Patil V, Sathaye S, Patil K (2014) *RSC Adv* 4:4094
28. Zhou X, Wan L, Guo Y (2013) *Adv Mater* 25:2152
29. Deosarkar MP, Pawar SM, Sonawane SH, Bhanvase BA (2013) *Chem Eng Process* 70:48
30. Hummers WS, Offeman RE (1958) *J Am Chem Soc* 80:1339
31. Yang X, Zhang X, Ma Y, Huang Y, Wang Y, Chen Y (2009) *J Mater Chem* 19:2710
32. Wang H, Cui L, Yang Y, Casalongue HS, Robinson JT, Liang Y, Cui Y, Dai H (2010) *J Am Chem Soc* 132:13978
33. Bai H, Li C, Shi G (2011) *Adv Mater* 23:1089
34. Li Z, Wu S, Ding H, Zheng D, Hu J, Wang X, Huo Q, Guan J, Kan Q (2013) *New J Chem* 37:1561
35. Luo S, Xu X, Zhou G, Liu C, Tang Y, Liu Y (2014) *J Hazard Mater* 274:145
36. Li Y, Lv X, Lu J, Li J (2010) *J Phys Chem C* 114:21770
37. Seema H, Christian KK, Chandra V, Kim KS (2012) *Nanotechnol* 23:355705
38. Tang L, Nguyen VH, Lee YR, Kim J, Shim JJ (2015) *Synth Met* 201:54
39. Zhu Y, Wang Y, Xie J, Cao G, Zhu T, Zhao X, Yang H (2015) *Electrochim Acta* 154:338
40. Zhu J, Zeng G, Nie F, Xu X, Chen S, Han Q, Wang X (2010) *Nanoscale* 2:988
41. Qu J, Shi L, He C, Gao F, Li B, Zhou Q, Hu H, Shao G, Wang X, Qiu J (2014) *Carbon* 66:485
42. Liu H, Liu T, Dong X, Lv Y, Zhu Z (2014) *Mater Lett* 126:36
43. Tang XZ, Li W, Yu ZZ, Rafiee MA, Rafiee J, Yavari F, Koratkar N (2011) *Carbon* 49:1258
44. Lei Z, Ma G, Jia C (2007) *Catal Commun* 8:305
45. Zhang Q, Wen S, Lei Z (2006) *React Funct Polym* 66:1278
46. Lei Z, Wei L, Wang R, Ma G (2008) *Catal Commun* 9:2467